Lunar X-ray fluorescence observations by the Chandrayaan-1 X-ray Spectrometer (C1XS): Results from the nearside southern highlands

S. Narendranath [a,l,*], P.S. Athiray [a], P. Sreekumar [a], B.J. Kellett [b], L. Alha [c], C.J. Howe [b], K.H. Joy [d,k], M. Grande [e], J. Huovelin [c], I.A. Crawford [f], U. Unnikrishnan [a,l], S. Lalita [a], S. Subramaniam [a], S.Z. Weider [f,b], L.R. Nittler [g], O. Gasnault [h], D. Rothery [i], V.A. Fernandes [j], N. Bhandari [m], J.N. Goswami [m], M.A. Wieczorek [n], the C1XS team

[a] Space Astronomy Group, ISRO Satellite Centre, Vimanapura P.O., Bangalore 560 017, India
[b] STFC, The Rutherford Appleton Laboratory, Didcot, Oxon OX11 0QX, UK
[c] Division of Geophysics and Astronomy, Department of Physics, P.O. Box 48, FI-00014, 22 University of Helsinki, Finland
[d] Center for Lunar Science and Exploration, The Lunar and Planetary Institute, USRA, 3600, Bay Area Blvd., Houston, TX 77058, USA
[e] Institute of Mathematical and Physical Sciences, University of Wales, Aberystwyth, Ceredigion SY23 3BZ, UK
[f] Department of Earth and Planetary Sciences, Birkbeck College, Malet Street, London WC1E 7HX, UK
[g] Carnegie Institution of Washington, Department of Terrestrial Magnetism, 5241 Broad Branch Road NW, Washington DC 20015CIW, USA
[h] Université de Toulouse, UPS-OMP, CNRS, IRAP, 9 Av. colonel Roche, BP 44346, F-31028 Toulouse cedex 4, France
[i] Department of Earth and Environmental Sciences, Open University, Milton Keynes MK7 6AA, UK
[j] Institute of Physics, University of Bern, Sidlerstrasse 5, CH-3012 Berne, Switzerland
[k] Centre for Planetary Science at UCL/Birkbeck, Department of Earth Sciences, Gower Street, London WC1E 6BT, UK
[l] Department of physics, University of Calicut, Thenjippalam, Kerala, India
[m] Physical Research Laboratory, Navrangapura, Ahmedabad 380 009, Gujarat, India
[n] Institut de Physique du Globe de Paris, Univ Paris Diderot, 4 Avenue de Neptune, F-94100 Saint Maur des Fossés, France

ARTICLE INFO

ABSTRACT

The Chandrayaan-1 X-ray Spectrometer (C1XS) flown on-board the first Indian lunar mission Chandrayaan-1, measured X-ray fluorescence spectra during several episodes of solar flares during its operational period of ∼9 months. The accompanying X-ray Solar Monitor (XSM) provided simultaneous spectra of solar X-rays incident on the Moon which are essential to derive elemental chemistry. In this paper, we present the surface abundances of Mg, Al, Si, Ca and Fe, derived from C1XS data for a highland region on the southern nearside of the Moon. Analysis techniques are described in detail including absolute X-ray line flux derivation and conversion into elemental abundance. The results are consistent with a composition rich in plagioclase with a slight mafic mineral enhancement and a Ca/Al ratio that is significantly lower than measured in lunar returned samples. We suggest various possible scenarios to explain the deviations.

1. Introduction

The chemical composition of Solar System bodies is one of the major clues to determining the history of the Solar System origin and evolution, therefore almost every planetary mission carries an experiment to map surface chemistry. The chemical composition of the lunar surface has been largely deciphered by means of returned samples from Apollo and Luna missions and orbital remote sensing measurements in the near-IR, visible, X-ray and gamma-ray wavelengths. Spectral reflectance measurements in the visible and near-IR have mapped the relative abundance of Fe and Ti on the lunar surface (through the near-IR absorption band of FeO, and the visible spectral slope which is sensitive to TiO$_2$ abundance; e.g. Lucey, 1998). The natural gamma-ray emission from K, U, and Th was used to map the lunar abundances of these elements (Lawrence et al., 1998; Prettyman et al., 2006). In addition, nuclear reactions caused by galactic cosmic rays, excite nuclei of major rock-forming elements such as O, Mg, Al, Si, Ca, Ti and Fe, which then de-excite, producing characteristic gamma-rays (Metzger, 1993). X-ray remote sensing can also measure signatures from these elements as the lunar surface emits X-rays characteristic of elements present when X-rays from the Sun (Yin et al., 1993.) excite them

through the process of X-ray fluorescence. Many experiments in the past have employed these three techniques to reveal lunar surface geochemistry. However, a consistent data set on global elemental maps still does not exist.

While spectral reflectance measurements in visible and infrared are primarily sensitive to the major elements Fe and Ti (only relative abundance), the difficulty in gamma-ray measurements has been primarily due to the high and uncertain background. In addition, there are complexities involved in modeling various physics processes that generate the observed signatures. In this context, X-ray remote sensing provides a platform for unambiguous and unique identification of signals from the major elements and estimation of abundance and provides independent measurements to compare to abundances derived from gamma-ray and spectral reflectance techniques.

Past XRF experiments have established the technique and provided estimates of relative abundances of Mg and Al. The Apollo 15 and 16 XRF experiments (Adler and Gerard, 1972; Adler et al., 1973a,b) estimated Al/Si and Mg/Si ratios over an area covering ∼10% (Clark, 1979) of the equatorial region on the nearside of the Moon. The D-CIXS instrument on SMART-1 detected major elements up to Fe (Grande et al., 2007; Swinyard et al., 2009) during bright solar flares but the detectors suffered extensive radiation damage en-route (SMART-1 spent approximately 19 months traveling to the Moon) preventing accurate quantitative analysis. Thus no measures of absolute elemental abundances were derived from any of these measurements. The X-ray Spectrometer on the Japanese spacecraft Kaguya also suffered radiation damage that resulted in degraded spectral capability (Okada et al., 2009). The Chandrayaan-1 X-ray Spectrometer (C1XS) (Grande et al., 2009; Crawford et al., 2009) flown on-board the Indian lunar mission Chandrayaan-1 (Bhandari et al., 2004; Goswami and Annadurai, 2009) provided the best opportunity to date for generating accurate global maps of most of the major elements in the lunar regolith. The X-ray Solar Monitor (XSM) alongside C1XS provided a simultaneous measure of the incident solar spectrum. C1XS measurements could not produce a global map because solar flares powerful enough to stimulate detectable surface fluorescence were few during this unusually prolonged solar minimum. Our current analysis indicates no distinct lines during quiet-Sun observations for single pixels. A new analysis has been initiated to address elemental signatures from cumulative data from multiple observations. Though thus limited, C1XS data obtained has still provided the best spectral and spatial resolution lunar XRF spectra to date.

Estimation of elemental abundance requires a thorough understanding of the instrument response, a good measure of the rapidly changing excitation spectrum and knowledge of various parameters that affect the X-ray fluorescence intensity from a sample. The C1XS instrument underwent a detailed pre-launch characterization from which we are able to model the lunar XRF spectrum well. Using laboratory experiments with known sample compositions, the methodology for the conversion of X-ray line flux to elemental abundance has been validated.

In this paper, we describe in detail, the C1XS data analysis procedure. We then apply this to the XRF spectra obtained during the brightest flare observed during the Chandrayaan-1 mission. The X-ray line intensities derived from spectral fits to the data are then converted to elemental weight % using a software based on the fundamental parameter approach (Criss and Birks, 1968; Tertian and Claisse, 1982; Rousseau and Boivin, 1998). Finally we suggest possible scenarios to interpret the differences between our results and known lunar sample compositions.

2. Chandrayaan-1 X-ray Spectrometer (C1XS) payload

2.1. C1XS detectors for lunar observations

C1XS is described in detail in Howe et al. (2009). Briefly, the instrument consisted of an array of Swept Charge Devices (SCD) (Lowe et al., 2001) operating in the 0.8–20 keV energy range. SCDs developed by e2v Technologies Ltd. can be thought of as one-dimensional X-ray CCDs with faster read out, larger area and good spectral resolution within a benign operating temperature range of −20 to 0 °C (143 eV at 5.9 keV at −15 °C).

There were 24 SCDs arranged as three planar modules with eight SCDs in each module. Together they provided a geometric area of 24 cm^2. The detection efficiency was 42% at 1.48 keV (Al Kα) (Narendranath et al., 2010). Gold-coated copper collimators placed above each SCD defined an opening angle of ±14.3° which resulted in an instantaneous ground pixel of 25 km × 25 km (Full Width at Half Maximum, FWHM) on the lunar surface (for the 100 km altitude orbit of Chandrayaan-1). In the later part of the mission when the spacecraft orbit was raised to 200 km, the ground pixel size increased to 50 km × 50 km (FWHM). Two aluminum filters each of 0.2 μm thickness was employed to block visible light from flooding the SCDs. An aluminum door protected the detectors from energetic protons and electrons during the passage through the terrestrial radiation belts en-route to the Moon. The door also housed 24 ^{55}Fe radioactive sources with a titanium foil, which illuminated all detectors when the door was closed. The calibration source yielded four X-ray lines at energies 4.5 keV, 4.9 keV, 5.9 keV and 6.4 keV (Ti Kα, Ti Kβ, Mn Kα, Mn Kβ) and enabled routine monitoring of changes in spectral resolution and gain on-board. The SCDs were passively cooled by means of heat pipes connected to a radiator facing cold space.

2.2. X-ray Solar Monitor (XSM)

An independent X-ray Solar Monitor (XSM) used a Si-PIN detector with a 13 μm Be window for simultaneously measuring the solar X-ray spectrum. XSM was mounted on the upper deck of the spacecraft such as to maximize exposure to the Sun in its wide field of view of 105°. The full disk solar spectrum in the range 1.8–20 keV was measured over an integration time of 16 s.

3. Instrument calibration

3.1. C1XS

Lunar XRF spectra are typically weak signals under the low solar activity condition that existed during the nine months of C1XS operation (28 November 2008 to 29 August 2009). Hence, in order to derive the maximum detection efficiency which provides the most accurate absolute X-ray line flux from lunar XRF spectra, it is necessary to model the energy-dependent spectral re-distribution function (SRF which is the mathematical characterization of the observed response of the detector to a mono-chromatic beam of photons). C1XS underwent extensive calibration measurements at the RESIK X-ray beam facility at Rutherford Appleton laboratory (RAL), UK. A Si-PIN detector calibrated at the electron storage ring at PTB/BESSY II was used as a transfer standard. The SRF and its dependence on energy and temperature were studied and the detection efficiency of the instrument with respect to the transfer standard was derived. The instrument response thus generated was implemented in the form of a response matrix compatible with the X-ray spectral analysis package XSPEC (Arnaud, 1996). C1XS calibration is described in detail in Narendranath et al. (2010).

Post launch calibration using the in-built ^{55}Fe sources were carried out four times during the mission. The FWHM of the SCDs increased from 153 eV before launch to 163 eV at 5.9 keV at $-8\,°C$ after being placed in the lunar orbit. This degradation is attributed to the proton irradiation received en-route during the $\sim$16 day journey to the Moon. We assume that the temperature dependence of the energy resolution follows that obtained on ground and thus re-derive the response matrix for various temperature ranges. Finally, the data obtained during solar flares provide a gain calibration at low energies from the Mg, Al and Si XRF lines.

3.2. XSM

The XSM shutter housed an ^{55}Fe source covered by a thin Ti foil which generated four lines (4.5 keV, 4.9 keV, 5.9 keV and 6.4 keV) for calibration at the start of every observation (switch on before entering the sunlit side of the orbit). Every data set begins with 400 s of calibration spectra from which gain and energy resolution at these four lines can be determined. The effective area of the detector is derived from the calculated detection efficiency curve convolved with the collimator response (measured on ground). The calibration of XSM and its in-flight performance is described in Alha et al. (2009).

4. Observations and data analysis

4.1. C1XS

There were two phases of observations during the mission life of Chandrayaan-1. During the first phase from November 2008 to April 2009, the spacecraft was at an altitude of 100 km above the lunar surface with an orbital period of 118 min. During the second phase from May to August 2009, the spacecraft was moved to a 200 km altitude orbit. This increased the orbital period to $\sim$130 min and the instantaneous ground pixel of C1XS to 50 km × 50 km (FWHM); defined by its collimator. When adding spectra across multiple ground pixels, lunar X-ray fluorescence signals were observed during solar flares as weak as A1 class at a spatial resolution of $\sim$500 km.

C1XS was in operation nearly continuously for a period of 9 months during which the instrument typically collected data only during the sunlit portion of the orbit. The operating temperature range for the instrument was required to be below $-5\,°C$ based to optimize observation time. Whenever the temperature exceeded this limit, C1XS detectors were automatically switched off allowing detectors to cool. When the temperature fell below a pre-set limit of $-9\,°C$ the system switched back to standard operating mode.

C1XS on-board data processing results in three types of data packets: 10, 11 and 12 as described in Table 1. Since the solar activity was low, all data were acquired in type 10 or type 11 mode. The time-tagged events in type 10 and 11 packets were binned into 4096 ADC channel spectra with an integration time of 16 or 32 s (corresponding to the time required to cover a 25 km or 50 km

Table 1
Data types in C1XS.

Data type	Mode	Count rate limits	ADC channels	Remarks
10	Time tagged	<320 events/s	4096	Binned into spectra on ground
11	Time tagged	<800 events/s	4096	Binned into spectra on ground
12	Spectral	>800 events/s	512	Spectra on board

ground pixel), on ground. The channels were converted to energy space using the relation

$$\text{Energy } (i) = \text{channel } (i) \times \text{gain} + \text{offset}$$

where offset is made equal to zero by shifting the spectrum across channels.

Since gain is temperature dependent, the appropriate gain value has to be determined for the average detector temperature for every 16 or 32 s spectrum. Ground calibration measurements provided the temperature dependence of gain (Fig. 1). The on-board temperatures of the SCDs are measured using temperature sensors located at the two ends of the array. We assume the temperature of the eight SCDs in the middle as an average of the measurements at the ends. The temperature data are available every 60 s, so we interpolate to derive temperatures for every 16 or 32 s interval. The gain corresponding to this temperature is taken from tabulated values. After gain correction, we rebin the spectrum from each SCD to a common energy scale and add spectra together. The added spectra in 4096 channels are further re-binned to 1024 channels (equally spaced in energy) to enhance statistics since we are dealing with low event rates during all flares observed by C1XS (brightest being the observation during a C3 flare). These data reduction steps are summarized in Fig. 2.

The summed spectra (all 24 SCDs) are added over time to enhance statistics when required. This results in a coarser spatial resolution on the lunar surface, but was necessary as many of the observations were during weak A and B class solar flares. A response matrix (which defines the instrument response required to de-convolve the incident spectrum) is generated (Narendranath et al., 2010) for the summed spectrum using the SRF and detector effective area. The spectrum is analyzed using the standard X-ray spectral analysis package XSPEC (Arnaud, 1996) with a suitable background model and response matrix. The X-ray line flux in the observed fluorescent lines are determined and flux uncertainties derived.

4.2. XSM

The X-ray events in XSM were integrated into 16 s spectra on-board. XSM along with C1XS was switched on $\sim$5 min before the spacecraft entered into the sunlit side of the orbit. The shutter on XSM remains closed in a calibration mode for 400 s after every switch on. Thus data from every orbit contain 400 s of calibration spectra after which the shutter opens to observe the Sun. The gain and energy resolution together with the effective area corrected for
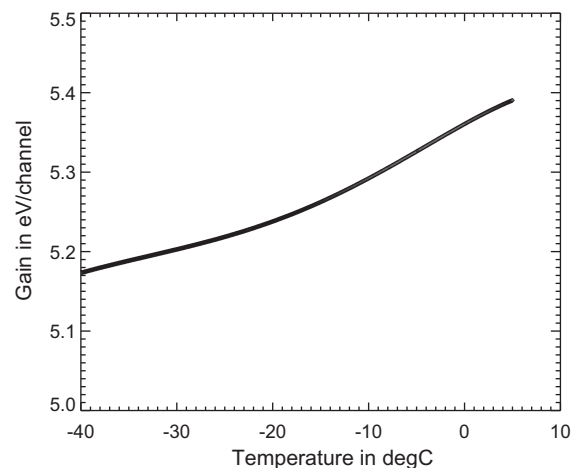

Fig. 1. Temperature dependence (interpolated from discrete measurements) of SCD gain derived from ground calibration data.

```
┌─────────────────────────┐
│ Raw data: time tagged   │
│ X−ray event list        │
└─────────────────────────┘
           │
┌─────────────────────────┐
│ Generate 16/32 s        │
│ spectrum as a FITS file │
└─────────────────────────┘
           │
┌─────────────────────────┐
│ Derive the peak channel of │
│ zero peak and shift to the │
│ zeroth channel          │
└─────────────────────────┘
           │
┌─────────────────────────┐
│ Using the temp dependent │
│ gain for each SCD, bin the │
│ spectrum into a common   │
│ energy scale with 1024   │
│ channels.                │
└─────────────────────────┘
           │
┌──────────────────┐   ┌─────────────────────────┐
│ Background Spectrum │   │ Add spectra across SCDs │
└──────────────────┘   └─────────────────────────┘
           │
┌──────────────────┐   ┌─────────────────────────┐
│ Detector efficiency │   │ Add spectra covering    │
└──────────────────┘   │ required time intervals │
                       └─────────────────────────┘
┌──────────────────┐             │
│ Instrument response │   ┌─────────────────────────┐
│  Spectral redistribution function │ Spectral analysis using │
│  Channel to energy calibration    │ XSPEC                   │
│  Spectral binning   │   └─────────────────────────┘
└──────────────────┘             │
                       ┌─────────────────────────┐
                       │ Derive X−ray line flux  │
                       └─────────────────────────┘
```
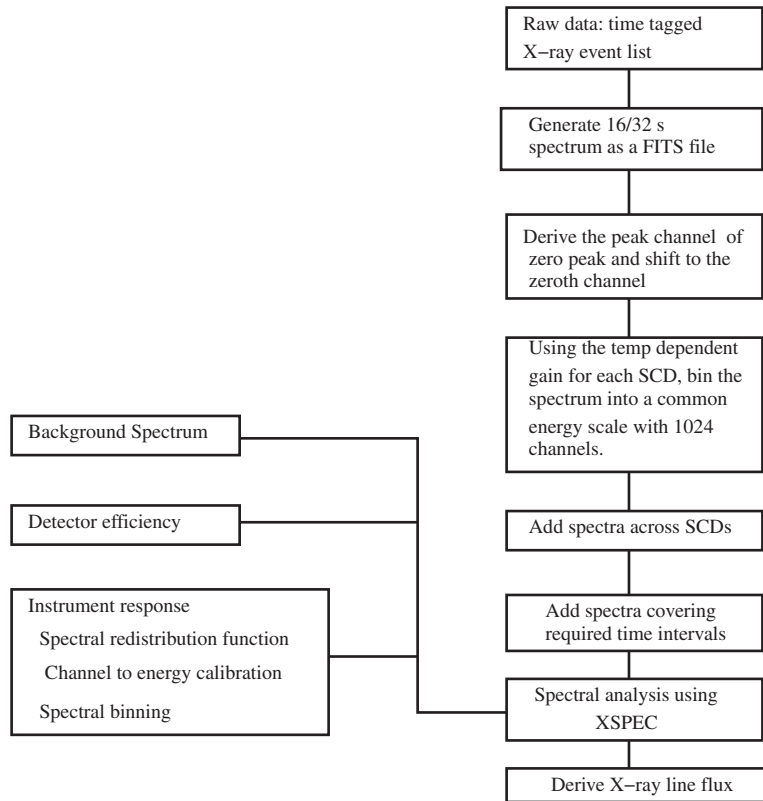
Fig. 2. Steps in C1XS data analysis. Background spectra are also processed in the same manner except for the last step (derivation of X-ray line flux).

off-axis pointing was used to generate a response matrix for analysis. We use OSPEX which is part of the standard solar spectral analysis package SolarSoft (SSW) (Freeland and Handy, 1998) for XSM spectral analysis.

In order to derive the absolute X-ray line flux in the observed XRF spectra from the lunar surface, the background in C1XS detectors and its variability needs to be understood. In the next section, we discuss the C1XS background observed in the lunar orbit.

5. X-ray background in the lunar orbit

The X-ray detector's background signal arises from internal and external sources. The internal source is the detector's dark current and the signal processing noise. The signal is usually dependent on temperature and increases due to cumulative radiation damage. The internal noise measured during ground calibration was found to be negligible for temperatures less than −5 °C. The external source is discussed in the following section.

5.1. Quiescent background

A featureless continuum background spectrum was measured by C1XS in lunar orbit. The average detector background count rate (∼3 counts/s per SCD) remains constant within 0.2% within an orbit as well as between orbits. This also implies that there are no significant temperature dependent variations in the detector background (−15 °C to −6 °C). We compared spectra obtained from the darkside with those obtained from the sunlit side and they are found to be very similar during quiet solar conditions. Spectra from the sunlit (solar quiet state) side and dark side are plotted together in Fig. 3. The major component of the observed lunar environment background arises from the interaction of high energy particles in
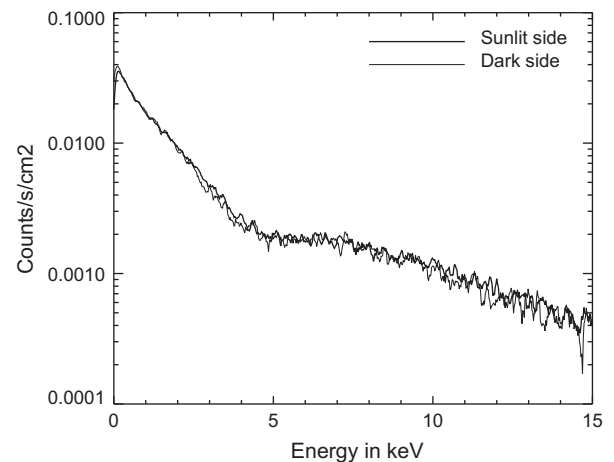

Fig. 3. Typical background in a C1XS–SCD in the lunar orbit at ∼−12 °C. The thicker line is the background when C1XS was on the sunlit (solar quiet condition) side and thinner line while on the darkside. This suggests low energy particle flux could largely contribute to the observed continuum background and that the scattered solar flux fraction is very small under these conditions.

the orbit with the detector and surrounding material. In the lunar orbit there is a continuous flux of protons and electrons with an energy range spreading from eV to GeV (geotail particles, solar cosmic rays and galactic cosmic rays). Lower energy particles directly interact with the detector, depositing energy and mimicking an X-ray event (Hall et al., 2008). Higher energy particles interact with the material surrounding the detector and generate secondary particles which could then deposit their energy in the detector under specific geometric configurations.

5.2. Detector background during geotail crossings

The Earth's magnetic field is stretched out into an elongated tail to distances of several hundred Earth radii in the anti-solar direction. It consists of oppositely directed field lines separated by a neutral sheet of plasma with a null magnetic field. Around this, is the plasma sheet which is dominated by electrons with an average energy of 1 keV (increasing to several keV occasionally; Prakash, 1975). In a synodic month (29.6 days), the Moon passes through the geotail in the 4–5 day period around full Moon.

C1XS observed a significant increase in the detector background with a harder continuum spectrum during some of the geotail crossings. A strong Al line (with no evidence of Mg or Si) whose strength varied over timescales of minutes was observed (Fig. 4) close to terminator (the imaginary circle dividing the sunlit and darkside) crossings of the spacecraft. This is believed to be due to Particle Induced X-ray Emission (PIXE) from the Al filter in front of the detectors and not lunar surface PIXE because of the absence of Mg and Si lines. Most likely the PIXE is induced by keV electrons dominating the geotail. It was generally observed that this Al line present at the terminator disappears after about 5 min into the sunlit side. The change in the spectral shape of the detector continuum background indicates the entry of the spacecraft into a region of different particle population (in energy) and higher flux.

The steady nature of the observed continuum background outside the geotail suggests that an average background spectrum can be used for spectral analysis except for observations inside the geotail. For observations inside the geotail, we use the pre-flare spectra and estimate the possible contribution from PIXE events.

6. Analysis of XRF spectra

We have carried out a detailed analysis of XRF data from C1XS during the brightest flare in the nine month observation period. A C3 solar flare that occurred on 5 July 2009 allowed simultaneous measurement of Mg, Al, Si, Ca and Fe from the lunar surface at a spatial scale of 50 km from the 200 km altitude of Chandrayaan-1 (second phase of the mission). Since measurements were made while in the geotail, we studied pre-flare spectra which show the occurrence of the Al line from the filter during terminator crossing. The brightest part of the flare occurred ~20 min (equivalent to
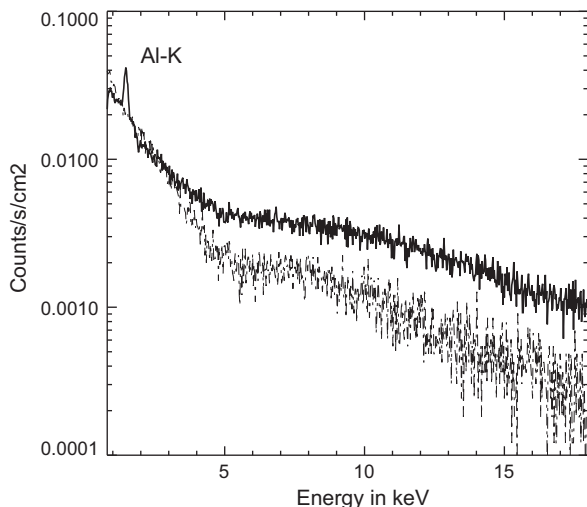

Fig. 4. The harder background spectrum (solid line) during a geotail passage compared to a nominal background spectrum (dotted line). The Al line excited from the Al filter by particles can also be seen with no evidence for Mg or Si implying that the emission is not from the lunar surface.

1872 km) away from the terminator and hence was not contaminated by the PIXE Al line. We used a spectrum from the pre-flare phase uncontaminated by Al filter line as background for lunar X-ray fluorescence spectra. The background subtracted flare spectra spread over five 50 km (FWHM) ground pixels (Fig. 5) were then fitted with a model consisting of a Gaussian function for the observed lines and a scattered solar spectral model for the residual continuum (explicitly shown in Fig. 6). We used the solar spectral model derived from XSM data for the given observation interval to calculate the scattered solar component. Initially the scattering surface was assumed to be represented by an average feldspathic terrane composition (Korotev et al., 2003). The normalization of this component was then allowed to vary to fit the observed continuum. The resulting abundance derived (discussed in the next section) were then used to re-estimate the scattered solar fraction. Convergence in the estimated abundance is usually achieved within two iterations.

The X-ray line flux determined for the C3 flare is compiled in Table 2. Plotted in Fig. 7 is the time variation in the X-ray line flux fraction (defined as the ratio of X-ray line flux from element *i* to the total line flux).

To first order, a flux fraction eliminates the dependence of solar intensity variations. However, in this work a more rigorous approach is adopted wherein the X-ray line flux values are converted to elemental weight % as described in the following section.

7. X-ray line flux to elemental weight %

The number of X-ray fluorescence photons produced from a sample, for a given incident spectrum of X-ray photons, can be calculated analytically. The work done by Sherman (1955) and further modified by Shirawai and Fujino (1966) shows that the number of primary X-ray fluorescent photons I_i (for an infinitely thick homogeneous sample) from an element *i* is given by:

$$I_i = \frac{1}{4\pi sin\,\psi_1} \int_{E_0}^{E_{max}} \frac{Q_{if}(E_0)I_0(E_0)\,dE_0}{\mu(E_0)cosec\,\psi_1 + \mu(E_i)cosec\,\psi_2} \tag{1}$$

where $I_0(E_0)$ is the incident spectrum, ψ_1 is the angle of incidence, ψ_2 is the angle of emergence, $\mu(E_0)$ is the total mass attenuation co-efficient (in cm²/g) for the energy E_0 and $\mu(E_i)$ for the energy E_i of the fluoresced element. Q_{if} is a measure of the fluorescent probability (*f*) for element *i* and can be calculated as follows.

$$Q_{if} = W_i\tau_i(E_0)\omega_{Ki}\frac{r_K - 1}{r_K}\omega_{Ki}f \tag{2}$$

In the above equation, W_i is the weight fraction of the *i*th element, τ_i is the total mass absorption co-efficient for the element *i*, ω_{Ki} is the K shell fluorescent yield of the *i*th element, $r_K \left(= \frac{\tau_{+}(\phi_K)}{\tau_{-}(\phi_K)}\right)$ is the K edge jump ratio. ϕ_K is the binding energy of an electron in the K shell. In a matrix of elements, the primary X-ray fluorescent photons can further interact with the atoms of other elements and produce secondary fluorescence (provided their energies are above the binding energy for electrons for the companion element) and even tertiary fluorescence. Shiraiwa and Fujino calculate the number of secondary and tertiary fluorescent photons generated in a matrix, in addition to the primary. The incident X-rays also interact with the sample via Rayleigh (coherent) and Compton (incoherent) scattering.

7.1. Factors affecting XRF intensity

The set of all elements in a sample is called a 'matrix'. The XRF line flux ($I_{obs}(i)$) from a particular element *i* is proportional to the number of atoms of the element present in the matrix and thus to the weight % W_i (the percentage by weight of a particular
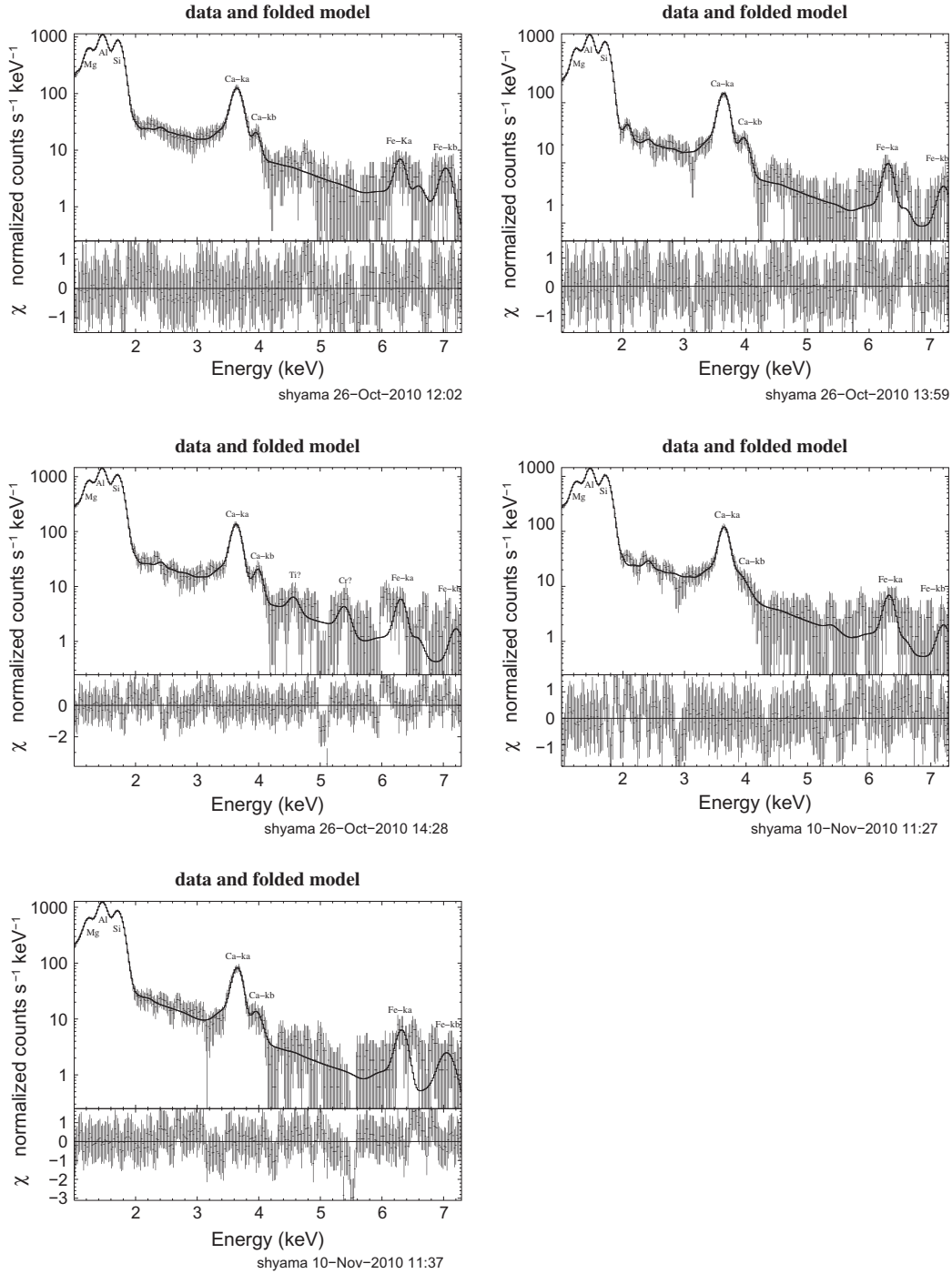
Fig. 5. Spectral fits to the five XRF spectra during the C3 solar flare along with the fit residuals (square root of the difference in χ^2 between model and data in each channel with a sigma of 1.) in the bottom panel. The model includes XRF lines and the scattered solar spectrum. Weaker signals from minor elements are also detected.

element with respect to all other elements in the sample). But $I_{obs}(i)$ does not vary linearly with W_i for the following reasons.

- $I_{obs}(i)$ is dependent on the incident spectrum which excites the sample.
- Matrix effects: If (N_i) XRF photons from an element i have energies greater than the binding energy of K shell electron of element j, then X-rays from element j are excited. Thus a fraction of the photons of element i is used to generate XRF photons from j. Element j is thus 'enhanced' and simultaneously intensity of i is reduced. Further, XRF photons from i and j could

get absorbed by the L shells of higher atomic number elements or K shells of lower atomic number elements in the sample resulting in a further reduction in N_i. Thus $I_{obs}(i)$ is sensitive to the 'matrix' of elements in the sample.
- Particle size: The lunar regolith being sensed remotely through X-rays contains a distribution of particle sizes ranging from cm-sized rocks to ultra-fine (<2 μm) particles (McKay et al., 1991). In regions where the mean particle size is larger than the penetration depth of X-rays (which is the case of lunar regolith), particle size affects the X-ray fluorescent line intensity. Laboratory experiments have shown that the X-ray fluorescent line
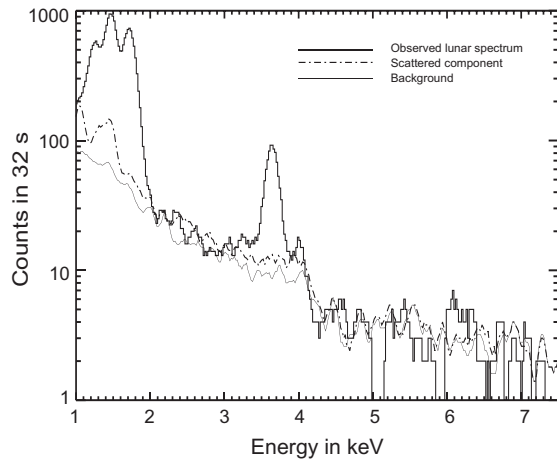
Fig. 6. Observed lunar spectrum along with the scattered component and background used to model the continuum.

intensity for a given element decreases with increasing particle size (Criss, 1976; Okada and Kuwada, 1997; Maruyama et al., 2008; Naranen et al., 2008; Weider et al., 2009).

- Homogeneity factor: If the grain size is larger than the mean free path of X-rays (10–15 μm for Mg, Al, Si and 100–200 μm for Ca, Ti and Fe) and the different elements are concentrated in different minerals (for example, Al in plagioclase and Mg in pyroxene and olivine), the sample cannot be considered homogeneous in the calculation (Nittler et al., 2001).
- Geometry of observation: X-ray fluorescence intensity is sensitive to the angle of incidence (ψ_1) of solar X-rays with respect to the lunar surface and to the phase angle (ϕ) (angle between the incident solar X-rays and the detector normal) (Okada, 2004; Naranen et al., 2008; Naranen et al., 2009; Weider et al., Submitted to publication).

Clearly, the observed line strength ($I_{obs}(i)$) of an element is not a direct measure of the true abundance. However, one can define a relationship between $I_{obs}(i)$ and a corrected line intensity $I_o(i)$ (which can be directly related to the true abundance of element i) as

$$I_{obs}(i) = f(S(E), i)[I_o(i) * M(S(E), E) * P(E, \psi_1, \phi, i)] \tag{3}$$

where $f(S(E), i)$ represents a function of the incident solar spectrum $S(E)$ for element i. $M(S(E), E)$ represents matrix effects, $P(E, \psi_1, \phi, i)$ includes cumulative effects of mean particle size and $*$ represents convolution. Inverting this equation does not yield unique solutions and hence as described below, we use a forward folding approach to derive the true composition. The incident solar spectrum is the most significant factor which affects the observed X-ray line intensity. Accurate modeling of the solar spectrum is thus crucial, in order to determine the element weight % from X-ray line flux.

7.2. X-ray fluorescence code

A knowledge of the fundamental physical parameters and the experiment geometry allows a direct calculation of the X-ray line intensity from any given material. This approach is widely used in laboratory experiments and yields fairly accurate results (Criss et al., 1978; Grieken and Markowicz, 2002). This has been extended to data from remote sensing XRF experiments for planetary surfaces. The planetary XRF experiments however lack the accuracy of laboratory experiments as the laboratory approach often involves well understood and controlled incident beam spectrum, beam geometry and standardized sample preparation against which to calibrate the observed X-ray line flux.

XRF experiments in the past have followed a methodology wherein the theoretical intensity from a sample composition is calculated analytically assuming a theoretically calculated solar spectral model. The Apollo 15 and 16 XRS experiments used solar X-ray flux from the Solrad 10 satellite and constructed a two temperature model (based on the assumption of a stable corona and an active spot) based on the work of Tucker and Koren (1971). Theoretical X-ray line intensities were calculated using a fundamental parameter method for a set of known lunar compositions which were then compared with the observed line intensities

Table 2
X-ray line flux in photons/cm²/s from C1XS spectral analysis of the C3 flare (5 July 2009) data. The central co-ordinates of each pixel are given in the first column.

| Lat, Long	Time in UTC	Mg Kα	Al Kα	Si Kα	Ca Kα	Ca Kβ	Fe Kα
−53.07, 8.22	07:04:44 07:06:50	0.18 ± 0.07	0.14 ± 0.04	0.37 ± 0.07	–	–	–
−46.97, 8.32	07:06:50 07:08:31	0.1 ± 0.06	0.04 ± 0.03	0.58 ± 0.1	–	–	–
−41.64, 8.394	07:08:31 07:10:10	0.18 ± 0.07	0.14 ± 0.06	0.42 ± 0.07	–	–	–
−39.44, 8.41	07:10:10 07:10:42	0.38 ± 0.18	0.75 ± 0.2	1.05 ± 0.2	–	–	–
−37.92, 8.43	07:10:42 07:11:14	0.57 ± 0.29	1.27 ± 0.2	2.3 ± 0.2	0. 4 ± 0.2	–	–
−36.39, 8.44	07:11:14 07:11:46	1.3 ± 0.3	3.6 ± 0.4	3.3 ± 0.3	0. 1 ± 0.04	–	–
−34.87, 8.45	07:11:46 07:12:18	3.3 ± 0.2	9.3 ± 0.3	6.9 ± 0.3	0. 1 ± 0.05	–	–
−33.35, 8.47	07:12:18 07:12:50	6.2 ± 0.3	18.3 ± 0.4	14.4 ± 0.4	2. 1 ± 0.2	0.4 ± 0.1	–
−31.83, 8.48	07:12:50 07:13:22	14.4 ± 0.9	23.7 ± 1.0	25.3 ± 0.8	3. 0 ± 0.1	0.25 ± 0.07	0.31 ± 0.07
−30.30, 8.49	07:13:23 07:13:55	19.1 ± 1.0	29.8 ± 1.1	29.8 ± 1.1	3. 3 ± 0.1	0.46 ± 0.08	0.53 ± 0.09
−28.78, 8.50	07:13:55 07:14:27	19.9 ± 1.1	27.8 ± 1.2	33.8 ± 0.9	2. 9 ± 0.1	0.28 ± 0.06	0.33 ± 0.07
−27.25, 8.52	07:14:27 07:15:00	20.8 ± 1.0	28.1 ± 1.1	31.2 ± 0.9	2. 6 ± 0.1	0.16 ± 0.05	0.26 ± 0.06
−25.74, 8.53	07:15:00 07:15:33	12.7 ± 1.1	27.6 ± 1.2	27.1 ± 0.9	1. 9 ± 0.1	0.24 ± 0.07	0.35 ± 0.06
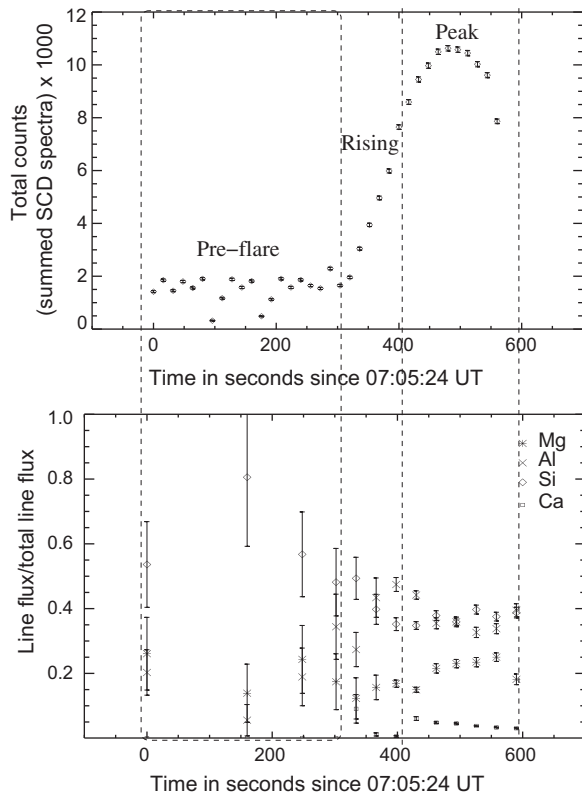
Fig. 7. Variation in X-ray line flux across lunar ground pixels (bottom panel) during the C3 flare. Line flux with large error bars are during the pre-flare times when line signatures are weak. The total counts in C1XS for the same time period is plotted in the top panel. Pixel to pixel variations suggest evidence for lunar chemistry variations at spatial scales of 50 km.

and the best match determined. A correction factor that is a function of the solar flux hardness ratio (a measure of the spectral variation) was derived, which relates the observed and calculated line ratios. Using this method, the Apollo experiments mapped about 10% of the equatorial region on the near side of the Moon (Adler et al., 1973a,b; Maxwell et al., 1977; Clark and Hawke, 1981, 1982, 1987, 1991).

The XRF experiment on Near Earth Asteroid Rendezvous (NEAR) used data from their solar monitor and accurately modeled the solar spectrum based on CHIANTI5.2 (Dere et al., 1997; Landi et al., 2006). This two temperature model was then used as input to their XRF code and elemental ratios derived based on the determination of the relationships between fluorescence ratios and elemental ratios from meteorite data (Trombka et al., 2000; Nittler et al., 2001; Lim and Nittler, 2009). Hayabusa XRF experiment used a standard sample plate to monitor the changes in the solar spectrum and derived surface elemental ratios for asteroid Itokawa (Okada et al., 2006).

The basic difficulty in all the earlier experiments has been the non-availability of a simultaneous solar spectrum with energy resolution good enough to accurately model the emission lines in the solar spectrum. The XSM on C1XS had the unique capability to measure the 1.8–20 keV solar continuum spectrum as well as to resolve some of the groups of emission lines superposed on the thermal continuum. The XSM can thus be used to generate a more accurate model of the solar spectrum.

We have implemented the fundamental parameter algorithm based on the X-ray fluorescence equation as given by Shirawai and Fujino (1966) including Rayleigh scattering. The difference with earlier approaches is that we calculate analytically the expected X-ray line flux for a set of matrices of elemental concentra-

tions covering a reasonably wide range, compare the calculated X-ray line flux fraction (line flux/sum of the flux in all lines) with the observed and then derive the best set of weight % using the method of least squares. Unlike other approaches where consistency with known elemental weight % is addressed, this approach derives the best combination of weight % that matches the observed X-ray line flux and known solar spectrum incident on the lunar surface. This means that we do not start with any presumed lunar compositions but arrive at the best values of weight % based on the observed X-ray line flux. A larger parameter space is searched in order to eliminate other local minima and to establish a smooth convergence. Further details of the XRF code and its validation against laboratory samples are given in Athiray et al. (in preparation).

8. Results

As stated earlier, to derive the elemental abundance from the X-ray line flux, it is necessary to accurately model the incident solar spectrum. XSM measured the incident solar spectrum simultaneously with C1XS XRF observations of the lunar surface. The groups of emission lines from highly ionized atoms of S (~2.4 keV), Ca (~3.8 keV) and Fe (~6.7 keV) are observed. Thus XSM has the capability to determine changes in coronal abundance during the flare from the line intensity variations. A single temperature model seems to be sufficient to model the 1–8 keV solar spectra for this flare and hence we did not include a harder spectral component that is present in many solar flares. XSM spectra (for the time corresponding to C1XS observations) were fitted with a single temperature (*vthabund* in OSPEX which is a model based on CHIANTI5.2 (Landi et al., 2006)), varying the coronal abundance to obtain a best fit for the intensity of emission lines in the spectrum. Table 3 gives the solar spectral parameters derived for the peak phase of the C3 flare measured by XSM. Fig. 8 shows one of the spectral fits to the XSM spectrum.

We have determined the elemental weight % over the five bright ground pixels observed during the C3 flare (Table 4) with the best fit solar model derived from XSM for each pixel. As we lack a measurement of the oxygen and titanium line flux, we have kept the oxygen weight % fixed at 43.87% and Ti at 0.13% (based on an average feldspathic terrane composition from Korotev et al. (2003) for all the pixels). For other elements the range used during the final iteration is given in Table 4. The angle of incidence and phase angle during the observations are known and have been used in the calculation. These values are compared with the average composition of soils from Luna 20, Apollo 16 mission (Haskin and Warren, 1991) and that of an average feldspathic highland terrane (Korotev et al., 2003). Abundances derived from Lunar Prospector gamma-ray spectrometer though at coarser resolution (Mg, Al, Si, Ca and Ti at 152 km and Fe at 80 km FWHM, Prettyman et al., 2006) are also included for comparison.

In order to add confidence, the results from this code were verified with an independent analysis with a similar XRF (Nittler et al., 2001) code developed for NEAR-XRS. For a given geometry, incident solar spectrum and composition, the fluorescent flux fractions from both codes agreed within 10%.

Table 3
C3 solar flare parameters, emission measure (EM) and plasma temperature (*T*) derived from XSM spectral analysis.

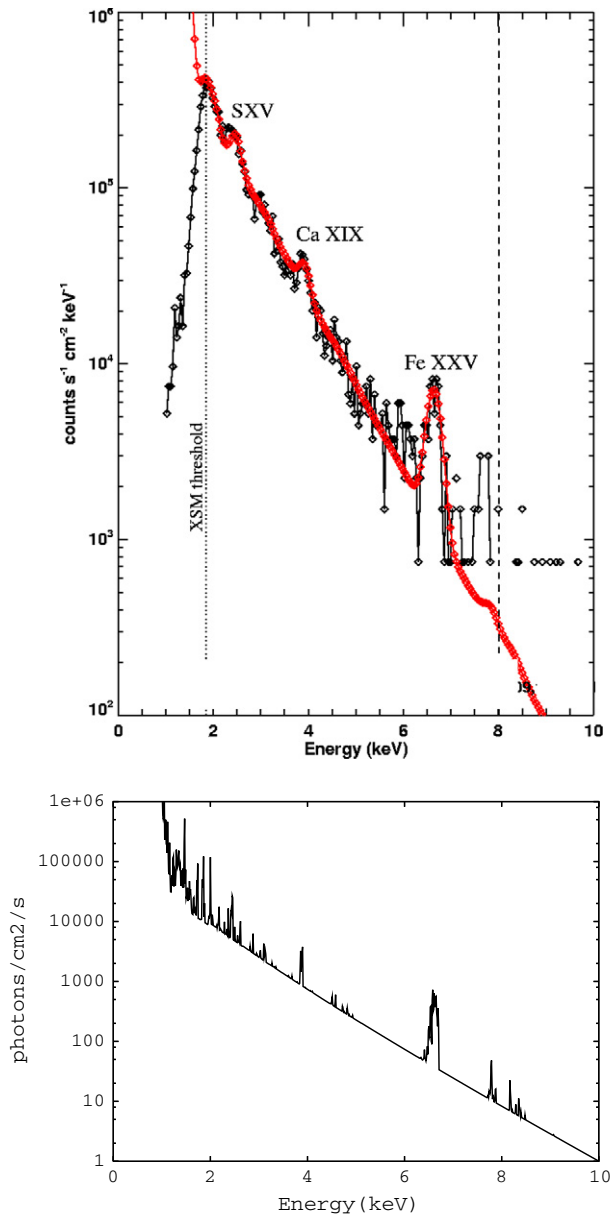| Time in UTC	EM × 10^{49}/cm^3	*T* (keV)	*T* (MK)
07:12:49–07:13:21	0.17 ± 0.005	1.15 ± 0.02	13.33 ± 0.23
07:13:21–07:13:53	0.22 ± 0.002	1.12 ± 0.01	12.98 ± 0.12
07:13:53–07:14:25	0.20 ± 0.002	1.10 ± 0.01	12.75 ± 0.12
07:14:25–07:14:57	0.18 ± 0.005	1.01 ± 0.01	11.71 ± 0.12
07:14:57–07:15:29	0.15 ± 0.002	0.95 ± 0.01	11.02 ± 0.12

Fig. 8. XSM spectrum for peak of the C3 flare fitted with continuum and line emission of an isothermal plasma (CHIANTI5.2). Groups of emission lines can be seen above the continuum. The unconvolved model spectrum is shown in the bottom panel.

9. Discussion

C1XS is the highest resolution, most accurately calibrated X-ray spectrometer flown to carry out global mapping of lunar chemistry. C1XS observations have yielded for the first time, a simultaneous measurement of the five major rock-forming elements for a few 50 km × 50 km ground pixels.

The region sampled during the C3 (Fig. 9) flare lies on the southern nearside highlands of the Moon (~37 ° and 26 °S at ~9 °W longitude). C1XS footprints during this time are over plotted on the Clementine albedo map (750 nm) (Fig. 9). The area mapped is located on distal ejecta rays of the crater Tycho (one of the youngest of the 100 km sized craters on the lunar surface), likely to be dominated by ejected blocks, impact glass and disturbed local regolith. The ejecta could have compositional differences from the surrounding material on which they were emplaced. However global elemental maps from Lunar Prospector gamma-ray data (Prettyman et al., 2006) show little compositional heterogeneity in this area.

Fig. 10 show the C1XS derived elemental abundances along with that of soils (Morris et al., 1983; Haskin and Warren, 1991) from the nine sample return locations. For a given aluminum abundance, it is seen that CIXS compositions are slightly higher in Mg and Fe, and lower in Ca than typical soils.

Localized heterogeneity may explain why large area averaging deployed by C1XS in deriving global elemental chemistry across the Moon can lead to differences from spot measurements provided by return samples from Luna and Apollo mission. It is also possible that the southern highlands have a unique composition different from known feldspathic compositions. However, before we converge on a conclusion, it is important to examine various scenarios that can specifically explain the deviations in the observed C1XS composition. We begin by addressing potential limitations in the analysis that in principle could give rise to such differences and close with the most likely explanations to understand C1XS results.

9.1. Limitations in the analysis

- *Limitations in understanding instrumental response:*
  The spectral re-distribution function (SRF) of the SCDs is derived from ground calibrations carried out at a few discrete energies. To derive the instrument response covering the full energy range of 1–10 keV, it was necessary to interpolate SRF parameters derived for discrete energies across the entire energy range. The derived energy-dependent SRF was validated using three independent data sources: (1) ground calibration data where the full thick-target bremsstrahlung spectrum was

Table 4
Elemental weight % for the highland region with 2σ errors, compared against an average of the feldspathic meteorite compositions (Korotev et al., 2003), Luna 20, Apollo 16 soil averages (Haskin and Warren, 1991) and LP values from the gamma-ray spectrometer (Prettyman et al., 2006). The weight % range used to derive abundance is also given.

| Time	Lat, Long	Range	Mg	Al	Si	Ca	Fe	$\frac{MgO}{MgO+FeO} \times 100$
07:12:50–07:13:22	−31.83, 8.48	2–15	5^{+1}_{-1}	17^{+1}_{-1}	20^{+1}_{-1}	8^{+1}_{-1}	6^{+2}_{-2}	45^{+7}_{-7}
07:13:23–07:13:55	−30.30, 8.49	5–25	6^{+1}_{-1}	17^{+1}_{-1}	19^{+1}_{-1}	8^{+1}_{-1}	6^{+2}_{-2}	50^{+7}_{-7}
07:13:55–07:14:27	−28.78, 8.50	15–25	6^{+1}_{-1}	16^{+1}_{-1}	21^{+1}_{-1}	8^{+1}_{-1}	5^{+2}_{-2}	54^{+8}_{-8}
07:14:27–07:15:00	−27.25, 8.52	4–15	6^{+1}_{-1}	15^{+1}_{-1}	20^{+1}_{-1}	9^{+1}_{-1}	6^{+3}_{-3}	50^{+7}_{-7}
07:15:00–07:15:33	−25.74, 8.53	2–12	4^{+1}_{-1}	18^{+1}_{-1}	17^{+2}_{-1}	6^{+1}_{-1}	11^{+1}_{-4}	27^{+7}_{-9}
Average feldspathic meteorite compositions			3.26	14.92	20.89	11.65	3.42	55
L20 (soil average)	3.5, 56.5 (landing)		5.84	12.04	21.13	10.51	5.8	56
A16 (soil average)	−9, 15.5 (landing)		3.62	14.41	20.98	10.41	3.87	55
LP	−31.8 to −25.7, ~8.5		5.4	14.3–10.8	20.6	11.6	4.7–5.5	56–59
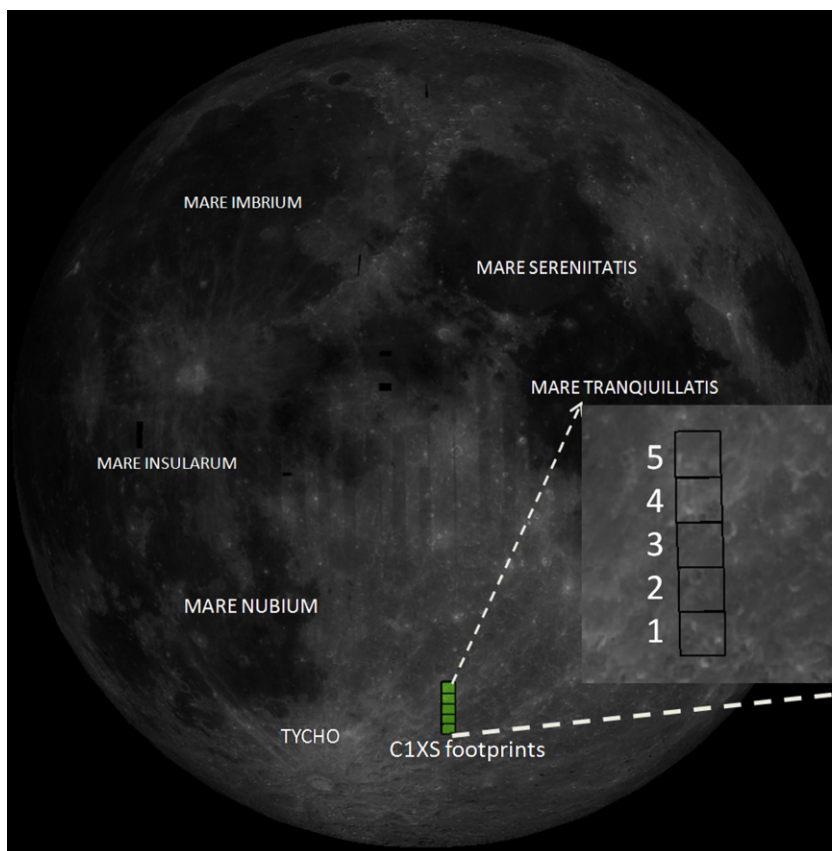
Fig. 9. General setting of the observed region (zoomed view in the inset).

obtained for the 2–10 keV range; (2) the four X-ray lines (4.5, 4.9, 5.9 and 6.4 keV) from the on-board calibration source, [55]Fe; (3) the observation of the Cosmic X-ray Background (CXB) emission (when the spacecraft was turned to observe Earth during solar eclipse of July 22, 2009). All three observed spectra could be fitted well with the standard SRF model, showing that the interpolation has not produced any artifacts.

Of the above tests, the observation of the CXB emission and reproduction of the well measured spectrum provides the most direct validation of the analysis process (Fig. 11). We derive the gain for typical lunar observations from the temp-gain table generated from ground analysis and validate this by extracting the correct line energies from the gain-corrected data. As the spacecraft was turned away from the Moon to observe Earth, the effect of not having the reflected heat load from the Moon appears to have made the standard temperature dependent gain correction factors less accurate for adding spectra from multiple SCDs. In this case we used the Ar line as a calibrator and find that the standard gain corrections for SCDs, is smearing the line. These Earth observations were too short to re-derive refined gain-correction factors for CXB spectra. Therefore a single SCD spectrum integrated over the observation duration is used. Though this did not provide adequate statistics to further constrain uncertainties in the detection efficiency determined on ground, these measurements conclusively indicated that there are no detector artifacts which would alter measured X-ray line intensities (eg: reduce the measured Ca line flux from the lunar surface). Though the detection efficiency has small uncertainties, since the overall continuum fit is satisfactory, any residual scaling of the detection efficiency, up or down, should not affect X-ray line flux fractions. Unlike the SCD response at energies greater than 2.3 keV where the complex

SRF model incorporates a significant contribution from split events, in the 1–2.3 keV range, the SCD response in our analysis is assumed to be characterized by a single Gaussian with the associated photopeak efficiency. The split events (expected to be small at low energies as the charge cloud radius is smaller and closer to the buried channel through which charge is transported) that may exist at these energies have been modeled as part of the continuum in the spectral analysis and hence should not affect X-ray line flux determination.

- Contribution from Particle Induced X-ray Emission (PIXE) from the Al filter on C1XS:
  Another possible internal source of line emission is from particle-induced X-ray emission process. The X-ray line at 1.49 keV arising from PIXE from the 0.4 μm thick filter on C1XS (used to block optical light) is observed during terminator crossings when the spacecraft is within the geotail where particle flux are expected to be higher. PIXE-produced Al line emission is seen for a short time span of a few minutes, 20 min before the flare and hence is adequately separated in time such that it should not affect the lunar Al X-ray line flux from the fully illuminated portion of the orbit. However the whole day of 5 July 2009, being a period of enhanced solar activity, it is possible that the local charged particle environment was very dynamic and enhanced during the lunar XRF observations. Although there is no evidence for an enhanced particle flux from the radiation monitor (RADOM) (Dachev et al., 2009) data on Chandrayaan-1 (whose energy range is above 800 keV), we cannot absolutely conclude that such an enhancement has not occurred at lower energies. However, the induced X-ray line flux from the Al filter observed during pre-flare terminator crossing time, is only 1.3% of the measured Al X-ray line flux from the lunar dayside. A PIXE contribution of more than 15% (nearly 10 times
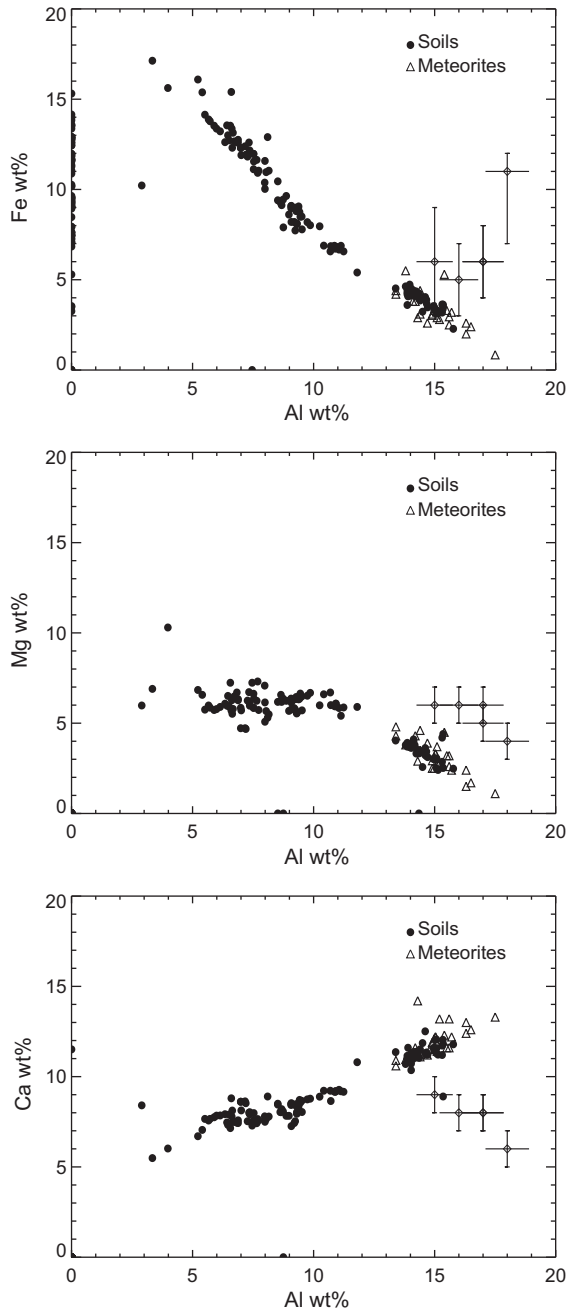
Fig. 10. Compositions derived from C1XS plotted along with lunar soil averages (Haskin and Warren, 1991; Morris et al., 1983) and feldspathic meteorite compositions (Demidova et al., 2007).
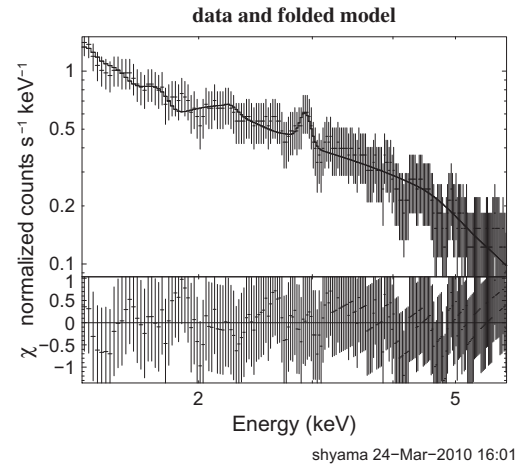

shyama 24–Mar–2010 16:01

Fig. 11. Cosmic X-ray background spectrum measured in C1XS fitted with a standard CXB model (Kushino et al., 2002) (hot diffuse gas emission, power law and a Gaussian line at 2.9 keV arising from the Ar fluorescence from Earth's atmosphere).

compositions (Athiray et al., in preparation). Earlier work (Nittler et al., 2001) suggests that effects of in-homogenous mixtures could alter the derived compositions significantly.

We estimated the flux fraction from a non-homogeneous mixture of the primary lunar highland minerals (87% plagioclase feldspar, 10% pyroxene and 3% olivine) and a homogenous sample of the same chemical composition. The ratio of the flux fractions from the in-homogenous and homogenous samples is a correction factor and was applied to the flux fractions estimated in our code to re-derive C1XS compositions. Table 5 gives the range in compositions derived from C1XS based on this correction. The first three pixels still have a Ca/Al ratio lower than typical feldspathic lunar regolith. It is to be noted that as the grain size decreases the effects of mixtures become negligible and the sample tends toward homogeneity. Hence the values in Table 5 should be seen as the extreme limits to the values given in Table 5.

As discussed earlier, particle size does affect the X-ray fluorescence intensity and has not been taken into account here. We calculated the average reduction in XRF intensity for lunar regolith (typical particle size distribution, McKay et al., 1991) as 30% for Mg–Si and 20% for Fe (calculated using values from Maruyama et al., 2008). The effect is partially eliminated by using flux fractions (line flux/sum of the flux in all lines) for deriving abundance as described in 6.2. The smaller change in flux at Fe contributes an uncertainty only within measurement errors.

So in conclusion, no convincing evidence exist to suggest that the non-standard composition has arisen from improper analysis or limitations in instrument or data modeling. We will now examine other scenarios to explain the observed composition.

stronger) to the Al line from the Moon would be required to lower the Al abundance to match typical highland composition. This appears highly unlikely.

- *Fluorescence X-rays from the Al filter:*
  X-ray photons emanating from the lunar surface can produce fluorescence of Al foils placed in front of the SCDs, enhancing the observed Al line intensity observed in C1XS. We calculated the contribution from the 0.4 μm Al to be 0.5% of the measured Al flux. Hence this cannot account for the enhanced Al flux we measure in C1XS.
- *Inversion of X-ray line flux to derive elemental weight %:*
  We follow a standard approach based on the fundamental parameter algorithm to derive the elemental weight % and the code has been validated with laboratory samples with known

Table 5
C1XS abundance limits between homogeneous and in-homogeneous model.

Time	Mg (%)	Al (%)	Si (%)	Ca (%)	Fe (%)
07:12:50–07:13:22	4–8	14–18	19–21	7–9	4–8
07:13:23–07:13:55	5–8	14–18	17–20	7–9	4–10
07:13:55–07:14:27	5–8	13–17	19–22	7–9	3–9
07:14:27–07:15:00	5–8	12–16	17–21	8–10	3–12
07:15:00–07:15:33	3–5	13–19	16–22	5–10	4–12

9.2. Compositional differences inherent to the Moon

It is generally believed that lunar highlands are mainly composed of plagioclase feldspar with lower amounts of mafic minerals. However none of the returned samples are from a purely feldspathic highland region and hence we cannot expect C1XS derived values to exactly match these. The higher Mg and Fe content derived here would arise from addition of mafic components redistributed by impacts. The major deviation in the C1XS derived values is Ca/Al ratio which for pure anorthite is 0.73. Addition of mafic components would raise this value whereas the Ca/Al ratio derived here is less than 0.7. We discuss below the possible explanations for this deviation.

- The Ca/Al ratio can decrease if the plagioclase feldspar is more sodic. Sodium content of 1-2% can explain the depletion in calcium in an area dominated by plagioclase. Data from a weaker flare (5 July 2009 05:05:01 to 05:07:54 UTC, decay part of a B2 flare) that illuminated an overlapping region (~30% overlap) of the same set of pixels observed by the C3 flare reveal the signature of X-ray fluorescence from sodium (Fig. 12).

Sodium line is observed during the brighter part of the flare and fades off as it decays. But we had to add the solar spectra for the whole observation in order to improve statistics. Spectral analysis of this added solar spectrum give a temperature of 6.9 MK and emission measure of 0.05×10^{49} cm^{-3}. We used the same analysis approach as for the C3 flare and derived abundances for Mg, Al and Si fixing the abundance of Ca, Ti and Fe to the values derived from the C3 flare. For the spectrum shown in Fig. 12,

Fig. 12. Spectral fit to the XRF spectrum during the B2 class (5 July 2009 05:05:01 to 05:07:54 UTC) flare showing the detection of XRF line from sodium. The contribution from scattered solar spectrum is plotted along with the lunar XRF data in the lower panel to show that the detected line cannot arise from any of the scattered solar coronal emission lines.

we get Mg: 3^{+3}_{-2}, Al: 12^{+7}_{-6} and Si: 24^{+6}_{-7}. Because of uncertainties in the detection efficiency at 1 keV, averaged solar spectrum and weaker XRF line flux, we are not able to constrain the Na abundance from this measurement.

The calculated scattered solar spectral component is plotted along with the observed lunar XRF spectrum in Fig. 12 to show that the detected Na signature cannot come from any of scattered solar coronal emission lines. We propose that the Na abundance on the surface soil could be thus greater than currently assumed thus enabling a detection through XRF.

Lunar samples typically have an anorthite content (defined as $\frac{Ca}{Ca+Na+K}$ in moles) as high as An$_{98}$ with the average highlands estimated to be An$_{95}$. Lower anorthite content (as low as An$_{70}$) (Wieczorek et al., 2006) plagioclase grains (and hence higher albite) have been found in lunar samples though rarer. Remote sensing measurements through which global lunar mineralogy has been studied, cannot identify the anorthite content unless the plagioclase is of the purest form (greater than An$_{98}$). Pure crystalline anorthosite (PAN) rocks distributed globally have been revealed by the Kaguya multi band imager (Ohtake et al., 2009), recently but surprisingly have never been identified in lunar samples. These PAN rocks have been identified from a weak absorption feature at 1.3 μm arising from trace amounts of Fe^{2+} incorporated into the mineral structure. This feature disappears if the material is shocked (by impacts). The band center position changes depending on the An content allowing its quantification (Wyatt et al., 2010). The majority of plagioclase on the Moon otherwise is identified by a featureless near-IR spectrum which does not reveal the An content.

Recent observations by the Diviner radiometer on LRO, which has three IR channels near 8 μm to measure the Christiansen feature (CF), has revealed regions where the band center shifts beyond their estimated range for the plagioclase, suggestive of the possible existence of higher amounts of albite (or sodic plagioclase) (Greenhagen et al., 2010).

- The technique of X-ray remote sensing, samples the very upper layer of the lunar regolith. The depth sampled depends upon the XRF photon energy (and hence the element), composition and density of the material. Assuming a density of 1.8 g/cm^3 and pure plagioclase feldspar all the major elements are being sampled from a depth <200 μm of the lunar surface.

The <10–20 μm fraction of the lunar regolith called the 'fines' are found to have a composition distinct from bulk regolith from which it was derived (Papike et al., 1982; Devine et al., 1982; Laul et al., 1982). Many of the fines are richer particularly in Al and Na (Papike et al., 1982). Apollo 16 soil 67461 exhibits mafic enrichment (Mg and Fe) and lower Ca in the fine (<10 μm) fraction (Papike et al., 1982).

If the upper (200 μm) layer measured consists mainly of this fine fraction, X-ray remote sensing would find a composition different from the bulk composition of the lunar samples (suggested by Basu (1985)). The lunar samples returned have always been collected as scoops and rock pieces and the very fine fraction is mostly lost. Even the core tubes intended to study stratification in the regolith have been compressed while the core tubes were hammered in and we do not know the possible layering in the upper tens of micron of the regolith. Recent examination of the beta cloth on the Apollo 16 Clam Shell Sampling Devices (CSSDs) that were designed to sample the top 100–500 μm of the lunar regolith suggest that the surface may contain a higher proportion of the less than 2 μm fines than the bulk soil (Noble, 2010). Mechanisms such as electrostatic levitation (Criswell, 1972), ballistic lofting and seismic shaking (Ostrach and Robinson, 2010) could over a long period of time, concentrate the fine fraction of the soil on the top layers. Thus C1XS observations could be revealing top surface
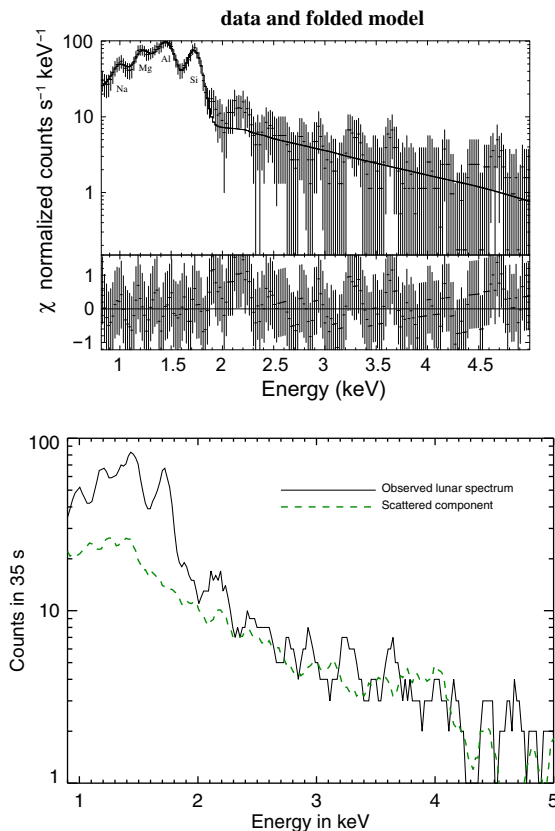
chemistry which would be deviant from the bulk. The data on fines especially on highland soil fines are sparse and hence we are not able to provide supporting evidences for this possibility.

The composition derived with C1XS data is thus not an 'experimental/analysis artifact' and requires more detailed modeling to provide conclusive evidences for the suggestions provided here.

10. Summary

In this paper we have described the methodology for X-ray spectral analysis of data from Chandrayaan-1 X-ray Spectrometer and presented the composition derived from for a region on the southern nearside highlands. This is the first direct simultaneous derivation of the abundance of five major elements (Mg, Al, Si, Ca and Fe) at a scale of 50 km. The compositions derived are distinct from lunar compositions found in returned samples. The high Al abundance is suggestive of a highland terrain with a mafic component, but the corresponding Ca is much lower than in the returned highland soils. We discussed the possible scenarios under which, such a deviation could occur. We showed that the analysis methods and instrument response modeling would not lead to this and suggest that this could be revealing regions of higher sodic plagioclase or indicating a different chemistry of the fines in the uppermost layer of the regolith. Continued analysis of C1XS data covering a larger region in the southern highlands would be more conclusive of the above results and provide a greater understanding of the processes involved.

11. The C1XS team

M. Grande, A. Cook, J.A. Carter (University of Wales, Aberystwyth, UK), B.J. Maddison, B.J. Kellett, C.J. Howe, B.M. Swinyard (STFC, RAL, UK), P. Sreekumar, A. Shrivastava, S. Narendranath (ISRO, India), J. Huovelin L. Alha (Helsinki Univ, Finland), I.A. Crawford, S.Z. Weider (Birkbeck College London, UK), K.H. Joy (LPI, USA) C.L. Duston, O. Gasnaut, S. Maurice (CESR, Toulouse, France), D. Smith (Brunel Univ., UK), D. Rothery, M. Anand, A. Holland, J. Gow (Open University, UK), S.S. Russell (Natural History Museum, UK), J.N. Goswami (PRL, India), N. Bhandari (PRL, India), D. Lawrence (Los Alamos National Lab, USA), V. Fernandes (Universidade de Lisboa, Portugal), T. Okada (ISAS, Japan), C. Erd (ESTEC, ESA), D. Koschny (ESTEC), C. Pieters (Brown University), M. Wieczorek (IPG Paris, France).

Acknowledgments

References

Adler, I., Gerard, J., 1972. The Apollo 15 X-ray fluorescence experiment. Geochim. Cosmochim. Acta 3, 2157–2178.
Adler, I. et al., 1973a. Results of the Apollo 15 and 16 X-ray experiment. Geochim. Cosmochim. Acta 3, 2783–2801.
Adler, I. et al., 1973b. Apollo 15 and 16 results of the integrated geochemical experiment. The Moon 7, 487–504.
Alha, L. et al., 2009. Ground calibration of the Chandrayaan-1 X-ray Solar Monitor (XSM). Nucl. Instr. Meth. A 607, 544–553.

Arnaud, K.A., 1996. XSPEC: The first ten years. ASP Conf. Ser. 101, 17–20.
Basu, A., 1985. Size compositional relationships in planetary regoliths and its role in interpreting remote sensing data. Meteoritics 20, 605–606.
Bhandari, N., Adimurthy, V., Banerjee, D., Srivastava, N., Dhingra, D., 2004. Chandrayaan-1 lunar polar orbiter: Science goals and payloads. Proc. Int. Lunar Conf. 108, 33–42.
Clark, P.E., 1979. Correction, Correlation and Theoretical Intensity Consideration of Lunar X-ray Fluorescence Intensity Ratios. PhD thesis. University of Maryland, Maryland, USA.
Clark, P.E., Hawke, B.R., 1981. Compositional variation in the Hadley Apenine Region. Proc. Lunar Planet. Sci. Conf. 12, 727–749.
Clark, P.E., Hawke, B.R., 1982. Geochemical classification of lunar highlands. Eos. Trans. AGU 63, 364.
Clark, P.E., Hawke, B.R., 1987. The relationship between geology and geochemistry in the Undarum/Spumans/Balmer region of the Moon. Earth, Moon Planets 38, 97–112.
Clark, P.E., Hawke, B.R., 1991. The lunar farside: The nature of highlands east of mare smythii. Earth, Moon Planets 53, 93–107.
Crawford, I.A. et al., 2009. The scientific rationale for the C1XS X-ray Spectrometer on India's Chandrayaan-1 mission to the Moon. Planet. Space Sci. 57, 725–734.
Criss, J.W., 1976. Particle size and composition effects in X-ray fluorescence analysis of pollution samples. Anal. Chem. 48, 179–186.
Criss, J.W., Birks, L.S., 1968. Calculation methods for fluorescent X-ray Spectrometry: Empirical coefficients vs fundamental parameters. Anal. Chem. 40, 1080–1088.
Criss, J.W., Birks, L.S., Gilfrich, J.V., 1978. Versatile X-ray analysis program combining fundamental parameters and empirical co-efficients. Anal. Chem. 50, 33–37.
Criswell, D.R., 1972. Lunar dust motion. Geochim. Cosmochim. Acta 3, 2671–2680.
Dachev, T., Tomov, B., Dimitrov, P., Matviichuk, Y., 2009. Monitoring the lunar radiation environment: RADOM instrument on Chandrayaan-1. Curr. Sci. 96, 544–546.
Demidova, S.I., Nazarov, M.A., Lorenz, C.A., Kurat, G., Brandsttter, F., Ntaflos, Th., 2007. Chemical composition of lunar meteorites and the lunar crust. Petrology 15, 386–407.
Dere, K.P., Landi, E., Mason, H.E., Monsignori Fossi, B.C., Young, P.R., 1997. CHIANTI – An atomic database for emission lines. Astron. Astrophys. 129, 149–173.
Devine, J.M., McKay, D.S., Papike, J.J., 1982. Lunar regolith: Petrology of the <10 μm fraction. J. Geophys. Res. 87, 260–268.
Freeland, S.L., Handy, B.N., 1998. Data analysis with the solar soft system. Sol. Phys. 182, 497–500.
Goswami, J.N., Annadurai, M., 2009. Chandrayaan-1. Curr. Sci. 96, 486–491.
Grande, M. et al., 2007. The D-CIXS X-ray Spectrometer on the SMART-1 mission to the Moon first results. Planet. Space Sci. 55, 494–502.
Grande, M. et al., 2009. The C1XS X-ray Spectrometer on Chandrayaan-1. Planet. Space Sci. 57, 717–724.
Greenhagen, B.T. et al., 2010. Global silicate mineralogy of the Moon from the diviner lunar radiometer. Science 329, 1507–1509.
Grieken, R.V., Markowicz, A., 2002. Handbook of X-ray Spectrometry. Marcel Dekker.
Hall, D., Holland, A., Turner, M., 2008. Simulating and reproducing instrument background for X-ray CCD spectrometers in space. Proc. SPIE 7021, 58–69.
Haskin, L., Warren, P., 1991. Lunar Source Book: A User's Guide to the Moon. Cambridge Univ. Press, Cambridge, England, pp. 357–474.
Howe, C.J. et al., 2009. Chandrayaan-1 X-ray Spectrometer (C1XS) instrument design & technical details. Planet. Space Sci. 57, 735–743.
Korotev, R.L., Joliff, B.L., Zeigler, R.A., Gillis, J.J., Haskin, L.A., 2003. Feldspathic lunar meteorites and their implications for compositional remote sensing of the lunar surface and the composition of the lunar crust. Geochim. Cosmochim. Acta 667, 4895–4923.
Kushino, A., Ishisaki, Y., Morita, Y., Yamasaki, N.Y., Ishida, M., Ohashi, T., Ueda, Y., 2002. Study of the X-Ray background spectrum and its large-scale fluctuation with ASCA. Publ. Astron. Soc. Jpn. 54, 327–352.
Landi, E., Del Zanna, G., Young, P.R., Dere, K.P., Mason, H.E., Landini, 2006. CHIANTI – An atomic database for emission lines VII: New data for X-rays and other improvements. Astrophys. J. 162, 261–280.
Laul, J.C., Papike, J.J., Simon, S.B., 1982. The lunar regolith: Comparative studies of Apollo and Luna sites. Chemistry of soils from Apollo 17, Luna 16, 20 and 24. Proc. Lunar. Planet. Sci. Conf. 12, 389–407.
Lawrence, D.J., Feldman, W.C., Barraclough, B.L., Binder, A.B., Elphic, R.C., Maurice, S., Thomsen, D.R., 1998. Global elemental maps of the Moon: The Lunar Prospector gamma-ray spectrometer. Science 281, 1484–1489.
Lim, L.F., Nittler, L., 2009. Elemental composition of 433 Eros: New calibration of the NEAR Shoemaker XRS data. Icarus 200, 129–146.
Lowe, B.G., Holland, A.D., Hutchinson, I.B., Burt, D.J., Pool, P.J., 2001. The swept charge device, a novel CCD-based EDX detector: First results. Nucl. Instr. Meth. A 458, 568–579.
Lucey, P.G., 1998. Model near-infrared optical constants of olivine and pyroxene as a function of iron content. J. Geophys. Res. 103, 1703–1713.
Maruyama, Y., Ogawa, K., Okada, T., Kato, M., 2008. Laboratory experiments of particle size effects on X-ray fluorescence and implications to remote X-ray Spectrometry of lunar regolith surface. Earth, Planets Space. 60, 293–297.
Maxwell, T.A., Strain, P.L., El-Baz, F., 1977. Mare crisium: Compositional Inferences from low altitude X-ray fluorescence data. Proc. Lunar. Sci. Conf. 8, 933–944.
McKay, D.S., Heiken, G., Basu, A., Blandford, G., Simon, S., Reedy, R., French, B.M., Papike, J., 1991. Lunar Source Book: A User's Guide to the Moon. Cambridge Univ. Press, Cambridge, England, pp. 285–356.

Metzger, A.E., 1993. Composition of the Moon as Determined from Orbit by Gamma-ray Spectroscopy. Remote Geochemical Analysis: Elemental and Mineralogical Composition. Cambridge Univ. Press, Cambridge, England, pp. 341–364.

Morris, R.V., Score, R., Dardano, C., Heiken, G., 1983. Handbook of Lunar Soils. JSC Publ. No. 19069. Planetary Materials Branch Publ. 67. NASA Johnson Space Center, Houston. p. 914.

Naranen, J., Parviainen, H., Muinonen, K., Carpenter, J., Nygard, K., Peura, M., 2008. Laboratory studies into the effect of regolith on planetary X-ray fluorescence spectroscopy. Icarus 198, 408–419.

Naranen, J., Carpenter, J., Parviainen, H., Muinonen, K., Fraser, G., Peura, M., Kallonen, A., 2009. Regolith effects in planetary X-ray fluorescence spectroscopy: Laboratory studies at 1.7–6.4 keV. Adv. Space Sci. 44, 313–322.

Narendranath, S., Sreekumar, P., Maddison, B.J., Kellett, B.J., Howe, C.J., Erd, C., Wallner, M., Weider, S.Z., 2010. Calibration of the C1XS Instrument on Chandrayaan-1. Nucl. Instr. Meth. A 621, 344–353.

Nittler, L.R. et al., 2001. X-ray fluorescence measurements of the surface elemental composition of asteroid 433 Eros. Met. Plan. Sci. 36, 1673–1695.

Noble, S.K., 2010. Examining the uppermost surface of the lunar regolith. Proc. Lunar Planet. Sci. Conf. 41, 1505.

Ohtake, M. et al., 2009. The global distribution of pure anorthosite on the Moon. Nature 461, 236–240.

Okada, T., 2004. Particle size effect in X-ray fluorescence at a large phase angle: Importance on elemental analysis of asteroid Eros (433). Proc. Lunar Planet. Sci. Conf. 35, 1927.

Okada, T., Kuwada, Y., 1997. Effect of surface roughness on X-ray fluorescence emission from planetary surfaces. Proc. Lunar Planet. Sci. Conf. 28, 1708.

Okada, T., Shirai, K., Yamamoto, Y., Arai, T., Ogawa, K., Hosono, K., Koto, M., 2006. X-ray fluorescence spectrometry of Asteroid Itokawa by Hayabusa. Science 312, 1338–1341.

Okada, T., Shiraishi, H., Shirai, K., Yamamoto, Y., Arai, T., Ogawa, K., Kato, M., Grande, M., and the Selene XRS team, 2009. X-ray fluorescence spectrometer (XRS) on kaguya: Current status and results. Proc. Lunar Planet. Sci. Conf. 40, 1897.

Ostrach, L.R., Robinson, M.S., 2010. Effects of seismic shaking on grain size and density sorting with implications for constraining lunar regolith bulk composition. Proc. Lunar Planet. Sci. Conf. 41, 2521.

Papike, J.J., Simon, S.B., White, C., Laul, J.C., 1982. The relationship of the lunar regolith <10 μm fraction and agglutinates. Proc. Lunar. Planet. Sci. Conf. 12, 409.

Prakash, A., 1975. Magnetospheric protons and electrons encountered by the Moon in the plasma sheet. The Moon 14, 71–78.

Prettyman, T.H., Jagerty, J.J., Elphic, R.C., Feldman, W.C., Lawrence, D.J., Mckinney, G.W., Vaniman, D.T., 2006. Elemental composition of the lunar surface: Analysis of gamma ray spectroscopy data from Lunar Prospector. J. Geophys. Res. 111, 12007–12048.

Rousseau, R., Boivin, J., 1998. The fundamental algorithm: A natural extension of Sherman equation. The Rigaku J. 15, 13–28.

Sherman, J., 1955. The theoretical derivation of fluorescence X-ray intensities from mixtures. Spectrochim. Acta 7, 283–306.

Shirawai, T., Fujino, N., 1966. Theoretical calculation of fluorescent X-ray Intensities in fluorescent X-ray spectrochemical analysis. Jpn. J. Appl. Phys. 5, 886–899.

Swinyard, B.M. et al., 2009. X-ray fluorescence observations of the Moon by SMART-1/D-CIXS and the first detection of Ti-Kα from the lunar surface. Planet. Space Sci. 57, 744–750.

Tertian, R., Claisse, F., 1982. Principles of Quantitative X-ray Fluorescence Analysis. Wiley.

Trombka, J.I. et al., 2000. The elemental composition of Asteroid 433 Eros: Results of the NEAR-Shoemaker X-ray Spectrometer. Science 289, 2101–2105.

Tucker, W., Koren, M., 1971. Radiation from a high temperature plasma: The X-ray spectrum of the solar corona. Astrophys. J. 168, 283–312.

Weider, S., Swinyard, B.M., Kellett, B.J., Howe, C.J., Joy, K.H., Crawford, I.A., Gow, J., Smith, D.R. Planetary X-ray fluorescence analogue laboratory experiments and an elemental abundance algorithm for C1XS. Planet. Space. Sci. Submitted to publication.

Weider, S.Z., Kellett, B.J., Howe, C.J., Joy, K.H., Crawford, I.A., Swinyard, B., 2009. C1XS surface roughness and phase angle experiments. In: Proc. X-ray Fluorescence Spectroscopy in Planetary Remote Sensing Workshop. Noordwijk, The Netherlands. SP-687-691.

Wieczorek, M.A. et al., 2006. The Constitution and Structure of the Lunar Interior. Rev. Min. and Geochem. 60, 221–364.

Wyatt, M.B., Donaldson Hanna, K.L., Paige, D.A., Greenhagen, B.T., Helbert, J., Maturilli, A., 2010. Diviner observations of pure plagioclase regions as identified by selene and the Moon mineralogy mapper. Proc. Lunar Planet. Sci. Conf. 41, 2498.

Yin, L., Trombka, J.I., Adler, I., Bielefeld, M., 1993. X-ray Remote Sensing Techniques for Geochemical Analysis of Planetary Surfaces. Remote Geochemical Analysis: Elemental and Mineralogical Composition. Cambridge Univ. Press, Cambridge, England, p. 341.